XII International Conference on Textile Composites and Inflatable Structures
STRUCTURAL MEMBRANES 2025
R. Wüchner, A. K. Goldbach, R. Rossi and C. Lázaro (Eds)

MATERIAL MODEL FOR RING ELEMENTS OF FLEXIBLE PROTECTION NETWORKS BASED ON SLIDING CABLE APPROACH

JOHANNA SIGENEGER* AND ROLAND WÜCHNER†

* Technische Universität Braunschweig
Institute of Structural Analysis
Beethovenstr. 51, 38106 Braunschweig, Germany
e-mail: j.sigeneger@tu-braunschweig.de, web page: https://www.tu-braunschweig.de/isd

† Technical University of Munich (TUM)
Chair of Structural Analysis
Arcisstr. 21, 80333 Munich, Germany
e-mail: wuechner@tum.de, web page: https://www.cee.ed.tum.de/st

Key words: ring element, flexible protection networks, sliding cable, material model, plasticity

Summary. This paper presents an approach to model protective ring nets using the Finite Element Method. The structural model is based on representing the rings with a sliding cable formulation. The development of a trilinear material model enables this structural model to capture not only the behavior of the rings when they are fully stretched but also when they are bending.

The material law can be calibrated for different ring types using load–displacement data from a single experimental setup. The transferability of the approach to other deformation modes is demonstrated with experimental data. Furthermore, this work provides an approach for discretizing the ring's mass in dynamic simulations and for visualizing the round shape of the ring during the bending phase.

1 INTRODUCTION

Climate change is increasing the occurrence and intensity of gravitational hazards such as rockfalls, debris flows, and mudflows, posing growing risks to both human lives and infrastructure. To mitigate these hazards, protective structures are commonly installed in mountain regions. Flexible protective systems not only offer aesthetic advantages over rigid structures but also possess the ability to absorb large amounts of energy through substantial deformations. Nets made of interconnected rings provide exceptional flexibility. Developing a numerical model for the simulation of ring nets can reduce the need for large-scale field tests. This would not only facilitate the design and safety verification of the nets but also make these processes faster, more sustainable, and cost-effective.

The behavior of such nets can be modeled using the Finite Element Method (FEM), in which each ring is discretized into elements. In the literature, several approaches to modeling ring behavior have been proposed. Escallon's[5] detailed beam-based model provides high accuracy but comes with significant computational costs, making it unsuitable for large net configurations. Nicot's[6]

center-interaction model is computationally efficient but neglects the ring geometry. Volkwein's approach uses a sliding cable formulation for the tension and diagonal springs to model the bending stiffness but was not further developed[4]. Grassl's model introduces intermediate nodes between contact nodes, allowing bending to be represented via rotational springs[7]. The formulation used in this work builds upon Boulaud's model[1], which is based on a sliding cable connecting only the contact points of the rings. This simple structural model reduces the number of degrees of freedom compared to Grassl's model by half but neglects important phases of the load-bearing behavior, as it only represents the ring behavior once it is already fully stretched.

In this document, a material model is developed to enable the sliding cable approach to also represent the ring behavior before the tension phase is reached in order to develop a ring element formulation, which is a favorable balance between computational efficiency and physical fidelity. Chapter 2 explains the material model. Chapter 3 describes its calibration for different ring types. Chapter 4 demonstrates the transferability of the calibrated material law to other deformation modes using the experimental data from Gottschang's tensile tests[2]. Chapter 5 introduces plasticity into the material model, and Chapter 6 discusses the discretization of the ring mass for dynamic simulations, particularly for the bending phase. Chapter 7 concludes the document with an outlook.

2 THE MATERIAL MODEL

As qualitatively illustrated in Figure 1, the rings show a non-linear load–deformation behavior in tensile tests. According to Volkwein, the load-bearing behavior can be divided into three phases: bending, rearrangement, and tension[3].

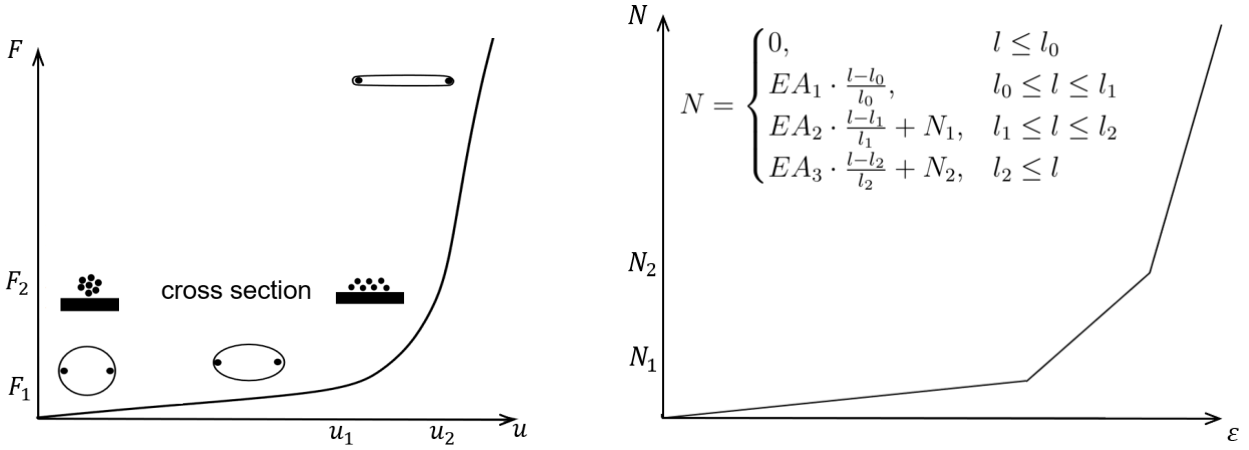

Figure 1: Qualitative load–deformation curve of a ring under uniaxial tensile loading (left, cf. Volkwein[3]) and its representation as a trilinear material law (right).

Initially, the ring undergoes bending. The curvature between the contact points decreases, while it concentrates at the contact points. Subsequently, the strands begin to shift at the contact points, causing the cross-section to flatten. In the final phase, the load-bearing behavior is governed by the elongation of the strands, and the ring behaves like a rope.

Boulaud's approach[1] neglects the first two phases of the load-bearing behavior. To enable the structural model of the sliding cable to also capture the bending and rearrangement phases, the load–deformation behavior observed in tensile tests is translated into a trilinear material law for the normal force. This is illustrated in Figure 1. The parameters relevant for the calibration of the material law are indicated in Figure 1 and further explained in Chapter 3.

In the net assembly, the rings avoid compression by shifting into each other. This behavior can be represented in the model by enforcing that the normal force cannot fall below $N_0 = 0$.

3 CALIBRATION

The material law can be calibrated using load–deformation data obtained from tensile tests, the setup of which is schematically illustrated in Figure 2. The relevant variable of the material law is the element perimeter l, which is calculated as the sum of the straight connection lengths between the nodes. These nodes represent the contact points of the rings and are therefore located on the inner side of the ring. The inner radius of the ring, r_{in}, is determined from the nominal radius minus half of the ring thickness.

The length l_0 is determined from the geometry in the unloaded state, using the bolt distances a_{Bolt} and b_{Bolt} as well as the bolt radius r_{Bolt}: $l_0 = 2(a_{Bolt} + b_{Bolt} + \pi r_{Bolt})$. It is assumed that the bending phase ends when the element length reaches the inner circumference of the ring, l_1. The corresponding displacement u_1, at which this condition is met, can be calculated from $l_1 = 2\pi r_{in} = l_0 + 2u_1$. From a displacement u_2, which results in the element length $l_2 = l_0 + 2u_2$, the load–displacement curve exhibits a linear behavior, marking the onset of the tension phase.

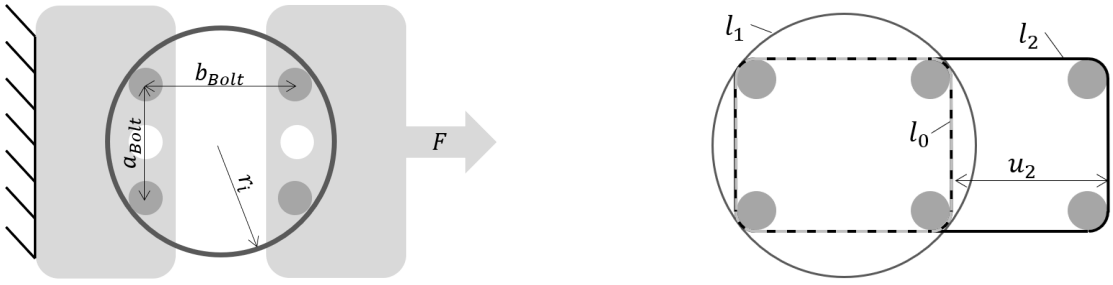

Figure 2: Setup of the tensile tests for calibration[2] (left) and illustration of the relevant lengths and their calculation (right).

Using the corresponding force values F_i for the relevant displacements u_i with $i \in \{1, 2\}$, which can be obtained from the load–deformation curve, the axial stiffnesses of the bending phase EA_1 and the rearrangement phase EA_2 can be calculated as

$$EA_1 = \frac{0.5 \cdot F_1}{\frac{l_1}{l_0} - 1} \quad \text{and} \quad EA_2 = \frac{0.5 \cdot (F_2 - F_1)}{\frac{l_2}{l_1} - 1}. \tag{1}$$

The tensile stiffness in the tension phase, EA_3, is calculated — following the approach proposed by Grassl and Volkwein[4] — from the tensile stiffness of the strands, using a correction factor.

4 VERIFICATION

Figure 3 shows a comparison of the load–deformation behavior from the tensile tests conducted by Gottschang[2] (in gray) with the corresponding simulations (shown as dots) for different test setups.

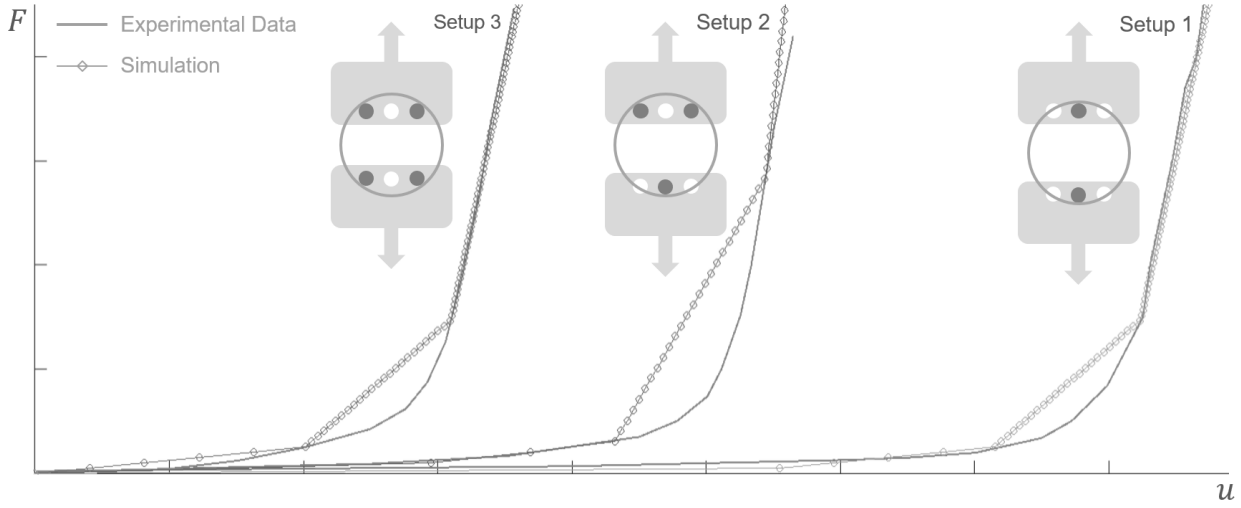

Figure 3: Comparison of simulation results with experimental data from Gottschang[2] for different setups.

With setup 3, in which the ring deforms into a square, the material behavior was calibrated. The simulation shows that the experiment can be well reproduced with this material behavior, as the simulation curve matches the experimental data at the relevant points. The same is observed when additional tests are simulated with the same material law. In setup 2, the ring is pulled into a triangle between three bolts, while in setup 1, it is stretched between two bolts.

The main difference in the load–deformation curves of the various setups occurs in the bending phase, since the length l_1 is reached at different displacements u depending on the shape. Overall, it can be concluded that the proposed approach is able to reproduce all shapes accurately.

5 PLASTICITY

Rings that have once been stretched should not be able to return to their original circular shape. Therefore, the material model is extended to include plasticity. The approach assumes that plastic moments develop during the rearrangement phase. While bending in Phase 1 and tension in Phase 3 remain elastic, the material behavior in Phase 2 is described as elasto-plastic. The hardening modulus corresponds to EA_2, and the elastic stiffness for unloading and reloading is assumed to be EA_3. Thus, the following relation holds

$$N = EA_3 \cdot \left(\frac{l}{l_{pl}} - 1 \right) = N_1 + EA_2 \cdot \left(\frac{l}{l_1} - 1 \right). \tag{2}$$

From this, the plastic element length can be calculated as

$$l_{pl} = \frac{EA_3 \cdot l \cdot l_1}{EA_2 \cdot (l - l_1) + l_1(EA_3 + N_1)} \tag{3}$$

within the limits $l_{pl,min} = \frac{EA_3 \cdot l_1}{EA_3 + N_1} \leq l_{pl} \leq \frac{EA_3 \cdot l_2}{EA_3 + N_2} = l_{pl,max}$.

During the Newton–Raphson iteration, a trial value $l_{pl,trial}$ is first calculated and compared with $l_{pl,max}$ and the plastic element length from the previous time or load step $l_{pl,prev}$. For case distinction, a temporary plastic flag marker is used, which is set to false at the beginning of each iteration step, as well as a permanent plastic flag marker that is set in the post-processing phase once equilibrium has been reached with $l \leq l_1$. This ensures convergence even around the discontinuity point at $l = l_1$. In the post-processing phase, the plastic length is also updated and then provided as $l_{pl,prev}$ for the next load or time step. However, its value can reach at most $l_{pl,max}$, so the material behavior in the tensile phase can be described as elastic. The following summarizes the individual cases:

$$N = \begin{cases} 0, & \text{compressive failure before plastification: plastic flag = false and } l \leq l_0 \\ EA_1 \cdot \left(\frac{l}{l_0} - 1\right), & \text{elastic bending: plastic flag = false and } l \leq l_1 \\ EA_2 \cdot \left(\frac{l}{l_1} - 1\right) + N_1, & \text{hardening: plastic flag = true and } l_{pl,prev} \leq l_{pl,trail} \leq l_{pl,max} \\ EA_3 \cdot \left(\frac{l}{l_{pl,prev}} - 1\right), & \text{elastic unloading and reloading: plastic flag = true and } l_{pl,trail} \leq l_{pl,prev} \\ EA_3 \cdot \left(\frac{l}{l_{pl,max}} - 1\right), & \text{elastic tension: plastic flag = true and } l_{pl,max} \leq l_{pl,trail} \\ 0, & \text{compressive failure after plastification: plastic flag = true and } l \leq l_{pl,prev} \end{cases} \tag{4}$$

6 DYNAMICS

The mass of the ring m_{ring} is distributed to the nodes using a lumped mass matrix. In the bending phase, the distribution is based on the arc approach, which is illustrated in Figure 4.

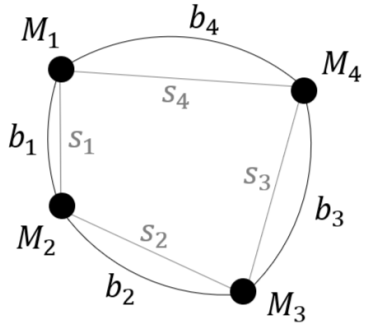

Figure 4: Visualization of the arcs and mass distribution in the bending phase

The curvature is assumed to be constant along the ring. Each ring segment s_i is associated with an arc of length b_i, which meets the arcs of the adjacent segments at the structural nodes under a

kink angle. All arcs have the same curvature radius r, which can be determined iteratively from Equation (5).

$$\sum_{i=1}^{n_{nodes}} b_i = 2r \arcsin\left(\frac{s_i}{2r}\right) = 2\pi r_{in}. \tag{5}$$

During the bending phase, the mass is distributed according to the arcs lengths. When the ring is stretched, the distribution can be performed in proportion to the segment lengths. The corresponding formulation is given in Equation (6).

$$M_i = \begin{cases} m_{ring} \cdot \frac{0.5\cdot(b_i+b_j)}{\sum_{i=1}^{n_{nodes}} b_i}, & l \leq l_1 \\ \\ m_{ring} \cdot \frac{0.5\cdot(s_i+s_j)}{\sum_{i=1}^{n_{nodes}} s_i}, & l \geq l_1 \end{cases} \quad \text{with } i \in 1, 2, \ldots, n_{nodes} \text{ and } j \in n_{nodes}, 1, \ldots, n_{nodes} - 1 \tag{6}$$

To visualize the rings in the bending state, the arcs are plotted based on the calculated curvature radius within planes defined by the respective segment and the geometric centroid of the structural nodes.

7 OUTLOOK

In this work, a material model was developed that enables the load-bearing behavior of rings to be modeled using the sliding cable approach. Compared to Boulaud[1], this also allows the bending and rearrangement phases to be represented. In contrast to Grassl's formulation, the presented method does not require the introduction of additional structural nodes, thereby halving the number of degrees of freedom and significantly reducing computation time.

Certain physical limitations remain within the current formulation. It should be noted that modeling bending through a normal force–strain law represents a physical simplification. To better capture the rigid-body deformation occurring in the bending phase, the reference length l_0 would ideally be calculated as a function of the ring deformation. Whether this refinement would result in a practically relevant improvement compared to the simplified approach remains uncertain. Another possible enhancement for modeling bending behavior could rely on the curvature radius, as described in the arc approach presented here. Ongoing work aims to investigate and implement such model improvements.

The procedure for calibrating the material law for different ring types using uniaxial tensile tests with lateral deformation restraint was described in detail so that it can also be adapted to future developments. Furthermore, the material model was extended to incorporate plasticity, enabling the representation of the dissipative work that plays a crucial role in flexible protection nets. This extension should be validated with further tests.

The proposed ring model shows convincing performance under uniaxial single-ring deformation. Nevertheless, additional experimental data are required – particularly from biaxial tensile tests and quasi-static out-of-plane tests on complete ring net assemblies. Performing such experiments would enable a verification of the modeling approach for the simulation of large scale ring nets and support its application in the design of real net structures.

REFERENCES

[1] R. Boulaud, C. Douthe and K. Sab: Modelling of curtain effect in rockfall barrier with the dynamic relaxation. International Journal of Solids and Structures, 2020, 200-201, pp.297 - 312.

[2] M. Gottschang: Trag- und Verformungsverhalten von ROCCO - Drahtringnetzen, Vertieferarbeit, Eidgenössisches Institut für Schnee- und Lawinenforschung, 2001

[3] A. Volkwein: Numerische Simulation von flexiblen Steinschlagschutzsystemen, Dissertation, ETH Zürich, 2004

[4] H. Grassl and A. Volkwein: Experimentelle und numerische Modellierung des dynamische Verhaltens von hochflexiblen Schutzsystemen gegen Steinschlag, Schlussbericht KTI-Projekt 4289.2.KTS, 2002

[5] J.P. Escallón , C. Wendeler, E. Chatzi and P. Bartelt: Parameter identification of rockfall protection barrier components through an inverse formulation, 2014

[6] F. Nicot, B. Cambou and G. Mazzoleni: Design of Rockfall Restraining Nets from a Discrete Element Modelling, 2001

[7] H. G. Grassl: Experimentelle und numerische Modellierung des dynamischen Trag und Verformungsverhaltens von hochflexiblen Schutzsystemen gegen Steinschlag. Doktorarbeit, ETH Zürich, 2002